H_2 and CO Production via Chemical Looping over Iron-Aluminium Oxides

Liisa K. Rihko-Struckmann[a]*, Pradyot Datta[a], Marcus Wenzel[a], Kai Sundmacher[a], N. V. R. Aditya Dharanipragada[b], Hilde Poelman[b], Vladimir V. Galvita[b], Guy B. Marin[b]

[a] Dr. L. K. Rihko-Struckmann*, Dr. P. Datta, M. Wenzel, Prof. K. Sundmacher
Process Systems Engineering
Max Planck Institute for Dynamics of Complex Technical Systems
Sandtorstr. 1, D-39106 Magdeburg, Germany
E-mail: rihko@mpi-magdeburg.mpg.de

[b] N. V. R. A. Dharanipragada, Dr. V.V. Galvita, Dr. H. Poelman, Prof. G. B. Marin
Laboratory for Chemical Technology
Ghent University
Technologiepark 914, B-9052 Zwijnaarde, Belgium

Abstract: Hydrogen and carbon monoxide production from H_2O and CO_2 is experimentally investigated using a two-step chemical looping process based on redox cycles of iron-alumina mixed oxides. The reduction of Fe_3O_4 in first endothermic step is followed by splitting of CO_2 or H_2O in a second exothermic step. The iron-aluminum oxides are more reactive with H_2O than with CO_2 in the range 650–750 °C. In situ XRD shows that deactivation results from different processes: iron oxide sintering and formation of spinel ($FeAl_2O_4$) with lower oxygen storage capacity. However, $FeAl_2O_4$ also takes over the role of Al_2O_3 and mitigates the iron oxide sintering. Deactivation at 650 °C is predominantly governed by sintering, while further loss of activity is due to combined sintering and spinel formation. At 750 °C the spinel formation is more dominant. A mixed oxide of Fe_2O_3 and Al_2O_3 with mass ratio of 70:30 was found most active and stable for H_2O and CO_2 splitting in chemical looping.

Introduction

Global energy consumption will increase in coming decades, at least twofold by 2050, due to economic growth and increasing population. Currently, there is no clear pathway to satisfy the increasing energy and chemical needs for society by using economically and environmentally sustainable processes. It is still expected that the majority of fuels and chemicals will be produced from fossil fuels, including the increased use of shale gas. An entwined problem of burning any fossil fuel is the release of CO_2.

Production of fuels from CO_2 and H_2O using solar light, in e.g. thermochemical cycles is a current topic of large scientific and industrial interest.[1] Thermal water splitting usually applies extensive thermal cycles leading to severe temperature stress for the equipment. In solar driven water splitting, the temperature is typically switched between the high temperature solid oxide reduction (2000 °C) and the sequential low temperature solid material re-oxidation (800 °C) to reach high a yield of hydrogen.

In addition to the thermochemical cycles, chemical cyclic processes have obtained extensive attention during the last few years.[2] The most common application is chemical looping combustion (CLC) where the key process is the

transfer of oxygen from air to the fuel compartment by a solid oxygen carrier material.[3] The exhaust gas from the fuel compartment in CLC has low N_2 concentration and it contains mostly CO_2 and H_2O, thus allowing inherent CO_2 capture by carbon sequestration technologies. The chemical looping approach can be applied for steam reforming where syngas is used for the reduction and steam for oxidation to produce H_2.[4] In the cyclic dry reforming, methane is used in reduction and target is the production of CO from CO_2 during oxidation.[5] In all cyclic solid-gas processes special attention should be given to the material stability over hundreds of cycles, but the latter aspect has received only moderate consideration in scientific literature.

Chemical looping with solar thermochemical cycles has been examined to reduce simultaneously CO_2 and H_2O to syngas using Zn/ZnO, FeO/Fe_3O_4[6], and Sn/SnO_2[7] redox pairs. For all of these samples, H_2O exhibited higher reaction rates compared to CO_2. A strong correlation between the input molar ratio of H_2O:CO_2 and the product molar ratio of H_2:CO was shown over the temperature ranges investigated. The syngas composition over CeO_2 was experimentally determined as a function of the molar co-feeding ratio: the range H_2O:CO_2 of 0.8 to 7.7, yielded syngas with H_2:CO molar ratios from 0.25 to 2.34.[8] For the Fe-Ba hexa-aluminate carrier clearly higher reactivity was reported for H_2O than for CO_2 in the chemical looping partial oxidation of methane.[9]

The success of these processes strongly relies on the physico-chemical properties of the oxygen storage material: it requires a high reduction/oxidation rate, long-lasting stability and resistance against phase transformations. The present contribution investigates the relationship between structural changes of the looping materials and the overall activity and stability of the CO_2 and H_2O splitting process. Pure and modified iron-aluminum oxides have been reported to be promising candidates for H_2O splitting by CO reduction including air oxidation.[10] The present contribution compares the applicability and longtime stability of iron-aluminum oxides in chemical looping processes. Iron-aluminum oxides with varying ratio of iron oxide and alumina were synthesized. The materials and the abbreviations used for the prepared samples are listed in Table 1. The samples were tested for two applications, where the desired products are generated during the oxidation step: 1) in the H_2O splitting half-cycle hydrogen is produced from steam, and 2) in the CO_2 splitting process carbon monoxide is generated during the solid material oxidation. For both applications, hydrogen was applied as reducing fuel.

Comparable approaches with hydrogen as reducing agent have been followed for the CO_2 activation with nanostructured iron[5], CeO_2-modified Fe_2O_3 materials[11], or for water purification with Mo-doped $CeZeO_2$-Fe_2O_3 mixed oxides.[12] It should be noted that for the reduction step the quality of hydrogen is not critical, and e.g. tar, impurity or CO contaminated hydrogen from biomass gasification could be used. Of course, any reducing feed can be applied in this stage of the chemical looping process, e.g. for combined chemical looping combustion and reforming, a tail gas mixture from a PSA unit.[13] With H_2O re-oxidation, the produced hydrogen can directly be used in many applications, e. g. low temperature fuel cells.[14] On the other hand, using CO_2 as re-oxidant leads to activation and utilization of CO_2 at low temperature.[15] Combination of both feeds can provide syngas with controlled ratio of CO/H_2, e.g. for Fischer-Tropsch synthesis.[16]

In the present contribution the activity of various iron-aluminum oxide materials was investigated by quantifying the H_2 and CO yield in the corresponding looping processes. Furthermore, special attention was given to the long-term stability by means of in-situ XRD characterization to get an indication of cyclic steady-state operation.

Results and Discussion

Material Characterization

An elemental composition of 47 wt. % Fe and 14 wt. % Al for the sample FeAl70:30 was measured by ICP-OES. The measured elemental contents correspond to a calculated oxide weight of 71.8 and 28.2 wt. % for Fe_2O_3 and Al_2O_3, respectively, which is close to the targeted nominal iron oxide–alumina ratio of 70:30. For the sample FeAl60:40 the measured iron and aluminum content of 39 and 19 wt. % gives the corresponding oxide weight of 60.8 wt. % and 39.2 wt. %. The ICP-OES analysis of these two exemplary samples confirmed that the targeted composition of the mixed oxides was satisfactorily achieved in the applied urea precipitation.

Table 1 lists the measured BET surface areas for the freshly calcined as well as for the used samples after the hydrogen production measurements with 100 cycles at 650 °C and 750 °C. A high surface area is not necessarily an indicator for a good oxygen carrier material, but as a part of the material characterization the method confirms successful synthesis. The BET specific surface areas were between 57 to 81 m^2/g for the fresh samples after the calcination. The initial BET surface areas for the present samples synthetized by urea precipitation are somewhat higher than the BET surface areas reported for iron oxide-alumina samples synthetized by co-precipitation. Exemplary, the samples FeAl80:20 and FeAl60:40 yielded BET surface areas of 80 and 81 m^2/g, whereas Kidambi *et al*. reported 10.9 and 19.0 m^2/g for nominally equal iron oxide-alumina samples prepared with a slightly different synthesis procedure.[10a]

The as prepared materials were characterized using powder XRD to determine the phases present (Fig. 1). The patterns revealed the presence of characteristic peaks of Fe_2O_3 in all samples. There were no diffraction peaks attributable to Al_2O_3 even at higher loadings, suggesting the amorphous nature of Al_2O_3. Further, there was no indication of $FeAl_2O_4$ in the as prepared samples. Indeed, the synthesis conditions do not favor spinel formation, as this requires high calcination temperatures (>1000 °C).[17] The average crystal sizes determined from the peak width of the four most intense peaks using Scherrer's equation lie between 33 and 22 nm for FeAl90:10 and FeAl60:40 respectively (Table 2). For increasing alumina loading, the Fe_2O_3 particle size is found to decrease indicating that alumina favors the iron oxide dispersion.

Isothermal Reduction

The reduction behavior of the calcined iron oxide-alumina samples was investigated isothermally at 800°C by following the temporal mass change. The samples were initially heated to 800°C under He atmosphere. A negligible mass decrease during the degassing and heating phase was observed (not shown). The reduction of the samples was observed in a few seconds as weight loss when the hydrogen was conducted into the TGA chamber. For FeAl90:10, 95 % of the experimentally observed total relative mass reduction (0.237) was achieved within the first 500 s. For the samples FeAl80:20, FeAl70:30 and FeAl60:40 the reduction progressed clearly slower (not shown here). However, the reduction was practically completed after 3600 s for all samples and beyond this time the observed mass decrease was negligible.

The detailed reduction behavior can be followed more clearly in the differential mass change illustration (see Fig. 2a). For the samples with lower alumina content FeAl80:20 and FeAl90:10, a two-step reduction behavior was observed during isothermal reduction: one around ~50 s and another broad change ~100 s after H_2 introduction. The samples FeAl60:40 and FeAl70:30 also showed a two-step reduction behavior, but with different rates as clearly seen in Fig. 2a. They reduced initially very fast during the first few seconds after H_2 introduction, yielding a very sharp differential mass change. Further reduction was however very slow and no other stages of reduction could be identified.

In order to identify the iron oxide phase changes and their evolution, in-situ XRD experiments were performed isothermally at 750 °C. The crystallographic changes in sample FeAl90:10 are represented in Fig. 2b. Initially, Fe_2O_3 transforms to Fe_3O_4 as intermediate phase after ~50s, followed by the transformation to FeO around 100s after the H_2 switch. Metallic Fe(110) at 44.7° diffraction angle appeared towards the end of the isothermal reduction in parallel to the FeO diffractions, hence the reduction remained incomplete. The latter could be due to the slightly lower temperature of 750 °C instead of 800°C employed here. Other samples follow the same trend (not shown). From comparison of Fig. 2a and b, it is likely that the first observed mass reduction for all samples includes both the initial reduction of Fe_2O_3 to Fe_3O_4 as well as the reduction of Fe_3O_4 to FeO_x, where x varies for wuestite between 0.9 and 0.95 for temperatures below 900 °C.[10a]

Assuming that initially only the iron oxide phase Fe_2O_3 is reducible, and the alumina phase remains unchanged under the hydrogen treatment in the isothermal experiment, we can analyze the achieved reduction degree of the solid material. Complete reduction of Fe_2O_3 to metallic Fe was expected. Under these assumptions, the sample with 10 wt. % alumina, FeAl90:10, could reduce by 27.1% leading to the final relative mass of 0.729, whereas the sample with highest alumina composition, FeAl60:40, could achieve only 18.0 % mass reduction ending up at a final relative mass of 0.820. Fig. 2c illustrates comparatively the degree of reduction in the TGA experiments for all samples and the theoretical maximal reduction degrees assuming complete Fe_2O_3 reduction to metallic Fe. All samples showed experimentally a slightly lower level of reduction than the calculated ones. Experimentally, the sample FeAl90:10 achieved 23.6 % reduction, when nominally 27.1 % could be expected. For the sample FeAl60:40 the corresponding values were 14.7 to 18.0 %, respectively. This is in agreement with the findings of Kidambi *et al.* as they reported that

for samples with 75 % Fe_2O_3 or less, the obtained degree of reduction was close to the expected value (Fe_2O_3 to Fe).[10a] However, a more pronounced deviation between the observed mass reduction and the expected one was reported by Kidambi *et al.* for samples with 50 and 60 wt. % Fe_2O_3 content. We did not observe such a clear differentiation in the reducibility as a function of the Fe_2O_3 content. All samples reduced to an extent between 80.6 (FeAl80:20) to 90.4 % (FeAl90:10) of the expected, theoretical value. However, it should be noted here that Kidambi *et al.* carried out typical thermogravimetric measurements by gradually increasing the temperature in contrary to our experiments where the reduction occurred isothermally at 800°C.

Activity for CO_2 Splitting

The activity of the solid materials was measured in a packed bed reactor. The CO_2 and water splitting with the synthetized materials were investigated separately. The CO_2 reduction was investigated at the temperature 750 °C with the samples FeAl90:10 and FeAl70:30. The solid material was able to reduce the CO_2 and generate gaseous CO during the CO_2 feed (step 4, see experimental). Fig. 3 illustrates exemplary the time course of the mass spectroscopy signals of m/z 44 (CO_2) and 28 (CO) during (a) the first cycle and (b) the 100th cycle for the sample FeAl90:10 at 750 °C. The illustration indicates a change in the kinetics of the solid material oxidation. Initially, during the first ten cycles (here is shown the first one), the oxidation of the material occurs fast and the CO concentration increases very sharply to a certain level. Thereafter, CO concentration decreases linearly. After 75 s the m/z 28 signal reaches a plateau (originating from the fractional mass of CO_2). During the cycles beyond about 20, the form of the CO peak changes into a less intense peak with a more gradual decay (Figure 3b).

Fig. 4 illustrates the quantified amount of CO as a function of the cycle number for samples FeAl90:10 and FeAl70:30 at 750 °C. The CO yield in the illustration is normalized to the initial mass of iron oxide (g_{Fe2O3}) in each mixed oxide sample. For FeAl90:10 the CO generation declined continuously over the repeated cycles and the quantified amount of CO decreased from the initial level of 2750 $mmol/g_{Fe2O3}$ to about 900 $mmol/g_{Fe2O3}$ after 100 cycles. The sample FeAl90:10 did not achieve a steady-state behavior during the 100 measured cycles. For the other investigated sample FeAl70:30 the CO generation initially dropped drastically during the first 10 cycles, but reached a close to steady-state level after about 20 cycles. Hereafter, this sample generated 1300 to 1100 $mmol/g_{Fe2O3}$ CO. It follows that an increased alumina content lowers the CO yield but is however beneficial for the material stability.

A more detailed structural and crystallographic analysis of the samples was carried out by in-situ time resolved XRD, which is shown in the following chapter.

Activity for H_2 Generation

The samples FeAl90:10, FeAl70:30 and FeAl60:40 were investigated for their ability to generate H_2 during oxidation of steam over 100 cycles as well. Fig. 5 shows the quantified amount of H_2 as a function of the cycle number at (a) 650 °C and (b) 750 °C. At 650 °C (Fig. 5a), the hydrogen amounts generated after 100 cycles over FeAl70:30 and FeAl60:40 were higher than those at 750 °C (Fig. 5b). For FeAl90:10, the activity at 750 °C was always above the one at 650 °C.

At both temperatures the sample FeAl90:10 showed a clear H_2 generation decline as a function of cycle number. No cyclic steady-state behavior could be observed unless towards the end of the 100 cycles. For the samples FeAl70:30 and FeAl60:40 the ability to split water was comparable to that for the CO_2 splitting. Here, a stable operation was achieved after about 20 cycles. For the lower reaction temperature, the hydrogen yield was on average 1700 $mmol/g_{Fe2O3}$ for the sample FeAl70:30 whereas the yield was in the range of 1100 $mmol/g_{Fe2O3}$ for FeAl60:40. At 750 °C, the hydrogen yield for these two samples was on average 1500 $mmol/g_{Fe2O3}$ and 700 $mmol/g_{Fe2O3}$, respectively. As for FeAl90:10, the yield decreased from 2250 to 475 $mmol/g_{Fe2O3}$ at 650 °C and from 5550 to 2400 $mmol/g_{Fe2O3}$ at 750 °C.

Due to thermodynamic limitation the stoichiometric maximal H_2 yield (18750 $mmol/g_{Fe2O3}$) is not achievable in steam oxidation. During the oxidation of FeO to Fe_3O_4 stoichiometric one could achieve maximally 4167 $mmol/g_{Fe2O3}$.

The observed yields are clearly lower than the calculated ones, with the only exception for the initial activity of FeAl90:10 at 750 °C. This indicates that the solid materials reached a kind of cyclic steady state under the applied experimental conditions, but the oxidation remained far from completed during each cycle. It should be mentioned here, that the duration of the reduction was kept constant in the experiments and the decrease in the oxygen carrying capacity might be due to limited rate of reduction. However, given the inexpensive raw materials applied in the present

study, the high stability makes the iron oxide-alumina materials economically interesting for the water and CO_2 splitting process despite the low yield.

In summary of the activity measurements the qualitative behavior of the investigated materials was comparable for both reactions. The inclusion of alumina contributes significantly to the stability. The sample with relatively low alumina inclusion, FeAl90:10, showed high initial activity, while the yield of the product molecules did not stabilize but decreased continuously over 100 cycles. In contrast to this, the samples with higher alumina inclusion FeAl70:30 and FeAl60:40 showed lower initial yield of the product molecules, but achieved a cyclic steady-state after about 20 cycles in terms of the H_2 and CO yield during the oxidation phase. The temperature 750 °C facilitated the formation of $FeAl_2O_4$ and lowered the H_2 yield on the long time (XRD diffractions for FeAl70:30 after 100 cycles shown in Figure 9).

In-situ XRD

The in-situ XRD cycling experiments allow tracing different phases of iron oxides and their evolution at constant temperature. The in-situ XRD pattern during cycling at 650 °C for the sample FeAl90:10 is presented in Fig. 6. During the first cycle, Fe_2O_3 transforms to FeO with Fe_3O_4 as intermediate phase during reduction. Metallic Fe (110) at 44.7° was not observed during the redox cycles at this temperature. During CO_2 re-oxidation, the FeO diffraction pattern changes into the one of Fe_3O_4. Diffraction peaks of $FeAl_2O_4$ were not observed in the in-situ 2D patterns.

From the 2D XRD window, the presence of $FeAl_2O_4$ cannot be evaluated adequately due to the limited angular resolution and possible overlap of peaks. Therefore, after seven redox cycles, the sample FeAl90:10 was cooled to room temperature and a full range XRD scan was recorded. This showed that the main constituent was Fe_3O_4 and no diffractions for $FeAl_2O_4$ were observed. All other samples follow the same trend during isothermal experiments at 650 °C, regardless of the Al_2O_3 loading (not shown).

The cycling experiments for the samples FeAl90:10 and FeAl70:30 at 750 °C are represented in Fig. 7. The reduction of FeAl90:10 starts by the conversion of Fe_2O_3 to Fe_3O_4 and further to FeO and Fe (Fig. 7(a)). Fe and FeO are oxidized to Fe_3O_4 during re-oxidation. In the subsequent cycles, the iron phase cycles between Fe and FeO during reduction and Fe_3O_4 upon re-oxidation. The in-situ XRD diffraction pattern of FeAl70:30 (Fig. 7b) shows that the reduction in the first cycle starts with Fe_2O_3 changing to Fe_3O_4, which is further reduced to FeO and Fe. The reduced phases are re-oxidized to Fe_3O_4. From the second cycle onwards however, FeO is found as most reduced iron phase.

As before, in order to check all compounds present, samples were cooled to room temperature after the 7-fold cycling and full XRD diffractions were recorded. Fig. 8 represents the part of an XRD scan where the spinel formation is most clearly observed (2Q = 56° to 67°). The diffraction curve corresponding to FeAl90:10 exhibits peaks with maximum intensity in the diffraction region of Fe_3O_4, i.e. 2Q = 57.1° and 62.7°, with only weak shoulders which could correspond to an intermediate phase between Fe_3O_4 and $FeAl_2O_4$. The XRD pattern for the sample FeAl70:30 however clearly shows the presence of intense peaks for $FeAl_2O_4$ formation, with minor contributions of Fe_3O_4.

The XRD patterns for the sample FeAl70:30 obtained after 100 cycles activity measurement at 650 °C and 750 °C are shown in Fig. 9. Characteristic peaks of Fe_3O_4 and $FeAl_2O_4$ are present in the samples at 650 °C, while close to complete formation of spinel is observed after the activity measurements with 100 cycles at 750 °C. The XRD pattern of FeAl70:30 now exhibits mainly diffractions of $FeAl_2O_4$ with only a slight asymmetry towards the angles of iron oxide, suggesting the presence of some remainder Fe_3O_4 (Fig. 9b).

The particle sizes for Fe_3O_4 after repeated redox cycles at the temperatures 650 °C and 750 °C have been tabulated in Table 2. The crystallite size of Fe_3O_4 at 650 °C and at 750 °C was determined using the two most intense peaks of Fe_3O_4 (2Q = 35.5° and 62.5°). After seven redox cycles at 650 °C, an overall increase in Fe_3O_4 particle size occurred for all samples, by a factor of two. The redox cycles at 750 °C increased the particle size even further for the samples FeAl90:10 and FeAl80:20 whereas with higher Al_2O_3 loadings, the crystallite size remained stable. After 100 cycles, the Fe_3O_4 particle size has further increased, especially for the FeAl90:10 sample.

TEM Analysis

HR-TEM was employed to study the structural changes, by comparing the initial and end state of the FeAl materials. The TEM images of FeAl90:10 and FeAl70:30 are shown in Fig. 10. For sample FeAl90:10, the TEM image of the as prepared sample (Fig. 10a) shows particles with an average size of ~30 nm. The post reaction HR-TEM micrographs after 7 and 100 cycles are shown in Fig. 10b and 10c, respectively. They show an overall increase in particle size after the cycled operation. The sample subjected to seven redox cycles reveals a particle size of ~65 nm while after 100 cycles it amounts to ~140 nm.

The TEM images of the fresh FeAl70:30 (Fig. 10d) exhibit a similar morphology with a particle size distribution around an average of ~25 nm. The TEM images after redox treatment (Fig. 10e and 10f) also exhibit an increase in particle sizes, with ~40 nm and ~78 nm after 7 and 100 cycles respectively. Average particle sizes determined from TEM are in agreement with the particle size ranges calculated from XRD (See Table 1).

The increase in particle size is attributed to sintering. However, as seen from comparison of FeAl90:10 and FeAl70:30, the phenomenon of sintering is reduced by loading more Al_2O_3, which acts as a physical barrier and hinders the physical contact between adjacent particles, thus preventing agglomeration. Hence, the average particle size remains much smaller in the samples with high amount of alumina.

Material Phase Changes during the Redox Cycles

The analysis of the XRD tests in combination with the activity measurements indicates that the observed deactivation of the FeAl samples in chemical looping is the result of two processes: 1) sintering, 2) spinel ($FeAl_2O_4$) formation.

The first is sintering of the active component which gives rise to an increase in particle size (Table 2). This process is always thermodynamically favored as two particles merge to form a new one leading to minimizing of the surface energy.[12a, 18] It results in an increased time of diffusion of oxygen atoms from the bulk to the surface, which in turn leads to a decrease of activity. However, this does not decrease the overall number of oxygen available for reaction.

This type of deactivation is observed during the redox cycling at 650 °C and 750 °C of FeAl90:10. The post reaction in-situ full XRD scan after cycling reveals no $FeAl_2O_4$ for this sample (Fig. 8). It must therefore be concluded that the amount of Al_2O_3 is too low to produce a detectable spinel phase. The steady loss of activity during cycling of FeAl90:10 is hence solely attributed to slow sintering of iron oxide (Fig. 4 and 5).

The XRD pattern after 100 cycles at 650 °C for FeAl70:30 (Fig. 9a) shows that here a spinel phase is present together with Fe_3O_4. The Fe_3O_4 particle size for this sample changes significantly in the first 7 cycles, but remains stable afterwards. Hence, the severe deactivation during first cycles at 650 °C is predominantly governed by sintering. Hereafter, the activity remains stable, indicating that the remainder Fe_3O_4 is less affected by sintering. Deactivation by spinel formation becomes more dominant at elevated reaction temperatures. This can be observed in FeAl70:30 after 7 cycles at 750 °C (Fig. 8), where spinel is really dominating the XRD pattern. Sintering also occurs during these first cycles, as the Fe_3O_4 particle size is found to increase (Table 2). During longer cyclic redox operation both sintering and spinel formation continue, yielding even larger particle sizes (Table 2) and almost complete spinel phase (Fig. 9b) after 100 cycles. Based on the CO and H_2 yields however, the largest drop occurs in the first cycles and a more stable performance sets in after 20 cycles, in contrast to sample FeAl90:10. This indicates that, while in the latter sample activity keeps on dropping due to continued sintering (no detectable spinel is formed), the further deactivation in FeAl70:30 is strongly suppressed after some cycles because of the spinel formation.

The formation of $FeAl_2O_4$ reduces the amount of active oxygen available for the desired reaction. The oxygen atoms bound in spinel contribute less to the material activity, hence the formation of the spinel phase is less favorable for the oxygen capacity of the sample. The amount of oxygen theoretically available calculated assuming all of the Al_2O_3 contributes towards the spinel formation is represented in Table 3. It shows that the amount of oxygen available for the desired splitting reactions after $FeAl_2O_4$ formation decreases by 9% for FeAl90:10 and as much as 52% for FeAl60:40 respectively (Table 3). Once all alumina is transformed into spinel, the activity in later cycles is ensured by the remainder Fe_3O_4, providing a stable though lower activity. As this Fe_3O_4 phase is not detected in the XRD patterns, it must be small-sized and well dispersed among the larger spinel particles. This possibly explains the more stable behavior against sintering.

Conclusions

A series of FeAl samples with different Al_2O_3 loading was prepared as oxygen storage materials for chemical looping processes in view of CO_2 and H_2O splitting. XRD of the resulting materials only showed Fe_2O_3 iron oxide as crystallographic phase. At increasing Al_2O_3 loading, the Fe_2O_3 particle size decreased and the BET surface area grew concomitantly.

All materials suffered from deactivation during prolonged cyclic operation in both splitting processes. For low Al_2O_3 loadings, this deactivation continued throughout the entire cycling process. For 30 wt. % Al_2O_3 loading and higher, however, the deactivation was essentially limited to the first 20 cycles, after which a more stable operation was established. Based on in-

situ XRD measurements and full ex-situ XRD scans in between and after cycling, the stabilization followed upon $FeAl_2O_4$ spinel formation, reducing the available amount of oxygen for cycling but preventing the iron oxide from further sintering.

Iron-aluminum mixed oxide is more reactive with H_2O than with CO_2 in the range 650–750 °C. The composition FeAl70:30 was found most active and stable for both H_2O and CO_2 splitting in chemical looping.

Experimental Section

Material Synthesis

The oxygen storage materials with varying mass ratios of Fe_2O_3 with Al_2O_3 were synthetized by urea precipitation. Initially, iron nitrate nonahydrate ($Fe(NO_3)_3{\cdot}9H_2O$, purity 99.99%, No 254223, Aldrich, Germany) and aluminum nitrate nonahydrate ($Al(NO_3)_3{\cdot}9H_2O$, purity 99+%, No 218285000, Acros Organics, Belgium) were dissolved in stoichiometric ratios at room temperature to obtain the precipitate compositions of four Fe_2O_3:Al_2O_3 mass ratios (90:10, 80:20, 70:30 and 60:40) The synthesis procedure is described in detail by Datta *et al.*.[12a] The solution was gradually heated to 100 °C to guarantee slow urea decomposition and controlled precipitation of the material. The mixture was kept overnight at 100 °C, and the precipitate was then separated by filtration and dried. Finally the samples were calcined in air at 650 °C.

Material characterisation

The elemental compositions of the fresh, calcined samples FeAl70:30 and FeAl60:40 were confirmed by ICP-OES (service from Currenta GmbH, Germany) to check the reliability of the precipitation synthesis method. The BET surface area of the prepared samples was determined by N_2 adsorption by a Quantachrom Instruments NOVA 2200e Analyzer (Quantachrom, Germany). The specific surface area (BET surface) was determined from five adsorption isotherm points at relative nitrogen pressures (p/p_0) between 0.05 and 0.3 by using the BET equation. The isothermal reduction experiments were carried out by following the weight change of a sample (10 mg) with TGA/SDTA 851 Analyzer (Mettler Toledo, Germany). During a reduction experiment at isothermal conditions at 800°C the gas flow was switched from inert gas (N_2, 120 ml/min) to 30 Vol. % H_2 in N_2 (total flow 120 ml/min) in the TGA furnace.

Activity investigation and the quantification of the product yield

The activity measurements were carried out at atmospheric pressure in a tubular quartz microreactor (i.d 8 mm) placed in an electric furnace. A material sample of 250 mg (particle size range from 280 mm to 560 mm) was packed between quartz wool layers in the reactor and the furnace temperature was controlled by a K-type thermocouple located between the oven and the quartz reactor. The total gas flow was always 120 ml/min (STP, 1 atm and 20 °C). The CO_2 reduction cycles were carried out with a repeated four-step program: step 1: flush with He during 7 min; step 2: reduction with 75 Vol. % H_2 balanced with He for 40 s; step 3: flush with He for 3 min; step 4: 83 ml/min (3.7 mmol/min) CO_2 balanced with He for 2.5 min. The water splitting cycles were carried out correspondingly with a four step program where the CO_2 treatment (step 4) was replaced with 4 g/h H_20 (3.7 mmol/min) balanced with He carrier gas. The product gas concentrations of H_2 (water splitting experiments) and CO_2 and CO (CO_2 splitting experiments) were monitored on-line using an MS Agilent 5973 Network Mass Selective Detector. During the experimental series, the response of the mass spectrometer detector was regularly controlled with a calibration gas mixture. From the m/z signal 28 the fraction originating from CO_2 was subtracted before the CO quantification.

In-situ time resolved and classical X-Ray Diffraction

The changes in crystallographic structure were investigated with in-situ XRD in $\theta-2\theta$ mode. A Bruker-AXS D8 Discover apparatus was used with Cu Kα radiation of wavelength 0.154 nm and a linear Vantec detector covering a range of 20° in 2θ with an angular resolution of approximately 0.1°. Time resolved XRD was recorded with a collection time of 10s. Temperature Programmed Reduction (TPR), Temperature Programmed Oxidation (TPO) and isothermal redox cycles were applied to identify the crystallographic phases and interpret their reducibility. The structural changes in the oxygen storage material were followed in a home-built reactor chamber with Kapton foil window for X-ray transmission. A 10 mg sample was evenly spread in a shallow groove of a single crystal Si wafer. Interaction of the oxygen storage material with the Si holder was never observed. The chamber atmosphere was pumped and flushed with a rotation pump (base pressure $\sim 4 \times 10^{-2}$ mbar) before introducing the reducing/oxidizing gas flow. The experiments were performed using 5% H_2/Ar for reduction, CO_2 for re-oxidation and He as inert purging gas in flowing gas stream conditions (60 ml/min). TPR and TPO were carried out at a uniform ramping rate of 30°C/min to reach 800°C followed by a 10 min dwell time. In-situ TPR was immediately followed by in-situ TPO.

The cycling experiments were performed isothermally at temperatures of 650 °C and 750 °C. During the isothermal experiments the reduction and oxidation sequences lasting for 4 min each were repeated for seven cycles. Helium was purged in-between oxidation and reduction sequences for 4 min. Afterwards, full XRD scans were recorded post reaction in He flow at room temperature. This procedure was repeated for all samples. Peak positions and widths were determined by means of a Gaussian function, fit to a XRD peak in a chosen range of 2θ around the peak of interest. Due to the low angular resolution of the linear detector, these values cannot yield accurate crystallite size and unit cell parameters, but they did allow tracing trends in a qualitative way.

The changes in crystallographic structure after the activity measurements were carried out with X'Pert PRO powder diffractometer (PANalytical, Germany) with Cu Kα radiation. The powder diffraction patterns were collected under normal atmosphere and temperature in a 2θ scan range from 10° to 80° and a step of 0.017° with 30 s counting time at each angle.

Transmission Electron Microscopy (TEM)

The morphological and structural properties were investigated using a high resolution transmission electron microscope (JEOL JEM-2200FS) operated at 200 kV. An aberration corrected TEM equipped with Schottky-type field-emission gun (FEG) and EDX JEOL JED-2300D was used to obtain high resolution images. Various TEM based techniques like High Resolution Transmission Electron Microscopy (HR-TEM), Scanning Transmission Bright Field (STEM BF) and Energy Dispersive X-ray analysis (EDX) were employed to identify morphology, particle size, elemental distribution and composition. Specimens were prepared by immersion of a lacey carbon film on a copper support grid into the as prepared powder. Particles sticking to the carbon film were investigated. A beryllium specimen retainer was used to eliminate secondary X-ray fluorescence in EDX spectra originating from the specimen holder.

Acknowledgements

This work was supported by the "Long Term Structural Methusalem Funding by the Flemish Government", the Fund for Scientific Research Flanders (FWO; project G004613N), the Interuniversity Attraction Poles Programme, IAP7/5, Belgian State – Belgian Science Policy. We also thank Dr. Vitaliy Bliznuk, Department of Materials Science and Engineering, Ghent University for his support with the HRTEM measurements, and Prof. Christophe Detavernier and Geert Rampelberg of the Department of Solid State Sciences, CoCooN, Ghent University, for access to and assistance with the in situ XRD equipment.

Keywords: CO_2 splitting • energy conversion • hydrogen • iron aluminium oxide • chemical looping

[1] a) G. Centi, S. Perathoner, *Chemsuschem* **2010**, *3*, 195-208; b) J. A. Herron, J. Kim, A. A. Upadhye, G. W. Huber, C. T. Maravelias, *Energy Environ. Sci.* **2015,** *8*; 126-157; c) C. L. Muhich, B. W. Evanko, K. C. Weston, P. Lichty, X. H. Liang, J. Martinek, C. B. Musgrave, A. W. Weimer, *Science* **2013**, *341*, 540-542; d) W. C. Chueh, C. Falter, M. Abbott, D. Scipio, P. Furler, S. M. Haile, A. Steinfeld, *Science* **2010**, *330*, 1797-1801.

[2] a) J. Adanez, A. Abad, F. Garcia-Labiano, P. Gayan, L. F. de Diego, *Prog. Energy Combust. Sci.* **2012**, *38*, 215-282; b) L.-S. Fan, L. Zeng, S. Luo, *AIChE J.* **2015**, *61*, 2-22; c) M. Rydén, A. Lyngfelt, *Int. J. Hydrogen Energy* **2006**, *31*, 1271-1283.

[3] a) Q. Imtiaz, A. M. Kierzkowska, C. R. Müller, *ChemSusChem* **2012**, *5*, 1610-1618; b) M. Ryden, M. Johansson, E. Cleverstam, A. Lyngfelt, T. Mattisson, *Fuel* **2010**, *89*, 3523-3533.

[4] R. D. Solunke, G. Veser, *Ind. Eng. Chem. Res.* **2010**, *49*, 11037-11044.

[5] M. Najera, R. Solunke, T. Gardner, G. Veser, *Chem. Eng. Res. Des.* **2011**, *89*, 1533-1543.

[6] A. Stamatiou, P. G. Loutzenhiser, A. Steinfeld, *Chem. Mater.* **2009**, *22*, 851-859.

[7] G. Levêque, S. Abanades, J.-C. Jumas, J. Olivier-Fourcade, *Ind. Eng. Chem. Res.* **2014**, *53*, 5668-5677.

[8] P. Furler, J. R. Scheffe, A. Steinfeld, *Energy Environ. Sci.* **2012**, *5*, 6098-6103.

[9] S. Bhavsar, M. Najera, R. Solunke, G. Veser, *Catal. Today* **2014**, *228*, 96-105.

[10] a) P. R. Kidambi, J. P. E. Cleeton, S. A. Scott, J. S. Dennis, C. D. Bohn, *Energy Fuels* **2012**, *26*, 603-617; b) C. D. Bohn, J. P. Cleeton, C. R. Mueller, S. Y. Chuang, S. A. Scott, J. S. Dennis, *Energy Fuels* **2010**, *24*, 4025-4033; c) W. Liu, M. Ismail, M. T. Dunstan, W. Hu, Z. Zhang, P. S. Fennell, S. A. Scott, J. S. Dennis, *RSC Adv.* **2015**, *5*, 1759-1771.

[11] V. V. Galvita, H. Poelman, V. Bliznuk, C. Detavernier, G. B. Marin, *Ind. Eng. Chem. Res.* **2013**, *52*, 8416-8426.

[12] a) P. Datta, L. K. Rihko-Struckmann, K. Sundmacher, *Mater. Chem. Phys.* **2011**, *129*, 1089-1095; b) P. Datta, L. K. Rihko-Struckmann, K. Sundmacher, *Fuel Process. Technol.* **2014**, *128*, 36-42.

[13] M. Ortiz, P. Gayan, L. F. de Diego, F. Garcia-Labiano, A. Abad, M. A. Pans, J. Adanez, *J. Power Sources* **2011**, *196*, 4370-4381.

[14] a) V. Galvita, T. Schroder, B. Munder, K. Sundmacher, *Int. J. Hydrogen Energy* **2008**, *33*, 1354-1360; b) V. Galvita, K. Sundmacher, *Chem. Eng. J.* **2007**, *134*, 168-174.

[15] V. V. Galvita, H. Poelman, C. Detavernier, G. B. Marin, *Appl. Catal., B* **2015**, *164*, 184-191.

[16] a) G. R. Kale, B. D. Kulkarni, K. V. Bharadwaj, *Int. J. Energy Res.* **2013**, *37*, 645-656; b) I. Iliuta, M. C. Iliuta, *Ind. Eng. Chem. Res.* **2013**, *52*, 16142-16161.

[17] a) A. N. Tsvigunov, V. G. Khotin, A. S. Krasikov, A. S. Vlasov, B. S. Svetlov, *Glass Ceram+* **1999**, *56*, 249-251; b) A. N. Tsvigunov, V. G. Khotin, A. S. Krasikov, T. B. Puzyreva, B. S. Svetlov, A. S. Vlasov, *Glass Ceram.* **1998**, *55*, 283-284; c) C. E. Meyers, T. O. Mason, W. T. Petuskey, J. W. Halloran, H. K. Bowen, *J. Am. Ceram. Soc.* **1980**, *63*, 659-663; d) P. H. Bolt, F. Habraken, J. W. Geus, *J. Solid State Chem.* **1998**, *135*, 59-69.

[18] V. Galvita, T. Hempel, H. Lorenz, L. K. Rihko-Struckmann, K. Sundmacher, *Ind. Eng. Chem. Res.* **2008**, *47*, 303-310.

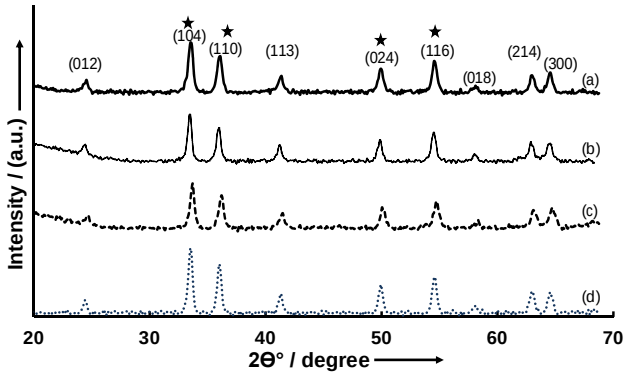

Figure 1. XRD diffractograms for the materials (as prepared) (a) FeAl90:10, (b) FeAl80:20 (c) FeAl70:30 (d) FeAl60:40. Peaks used the for crystal particle size calculation noted by stars.

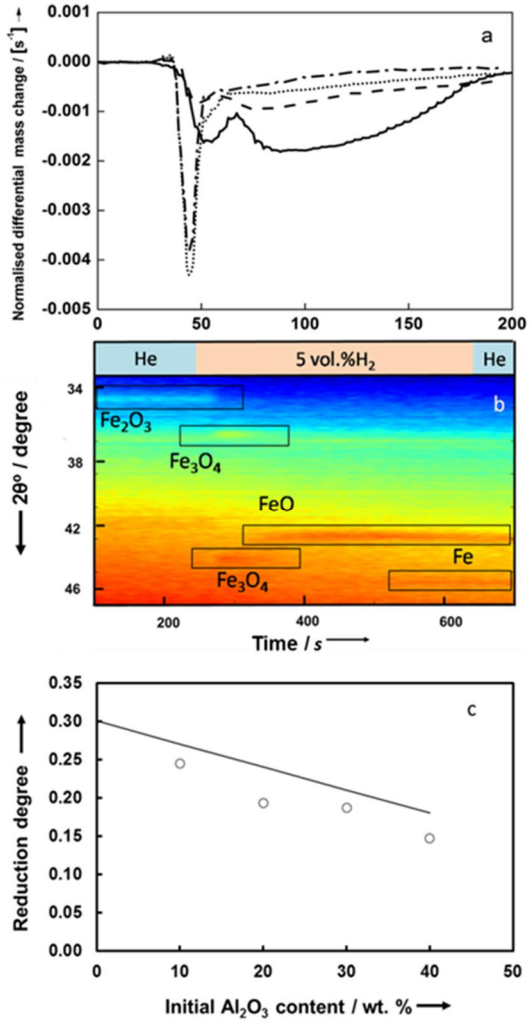

Figure 2. (a) differential mass loss during isothermal reduction by H_2 at 800 °C. solid: FeAl90:10, dashes FeAl80:20, dots: FeAl70:30, dash-dots:FeAl60:40, (b) Time resolved XRD pattern during reduction at 750 °C of FeAl90:10, c) theoretical (straight line) and observed reduction degree (○) from TGA for all FeAl samples.

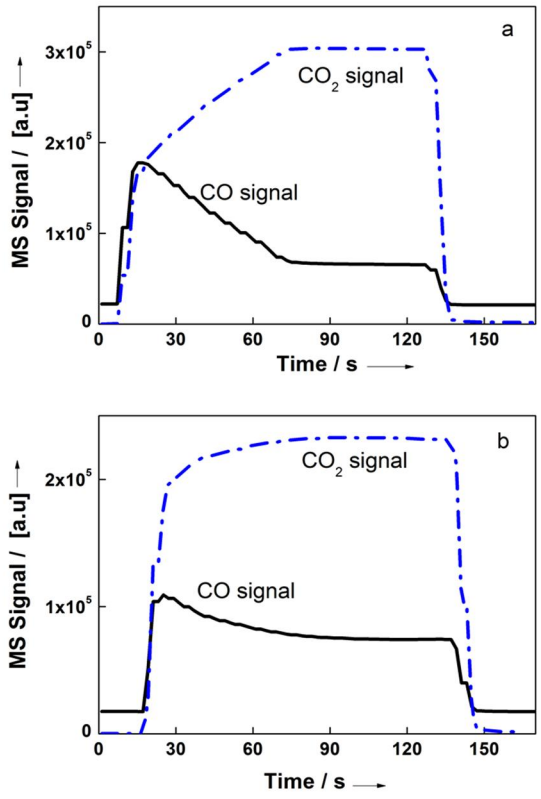

Figure 3. MS signals for CO_2 and CO, (a) first of 100 chemical looping cycles with alternating H_2 and CO_2 feed (b) 100th cycle for the sample Fe90:10 at 750 °C.

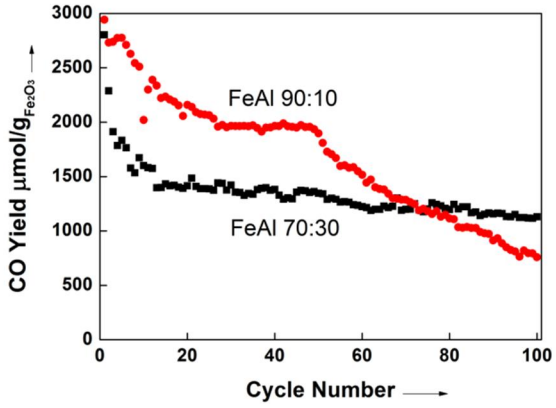

Figure 4. CO yield over 100 cycles for FeAl90:10 and FeAl70:30 at 750 °C.

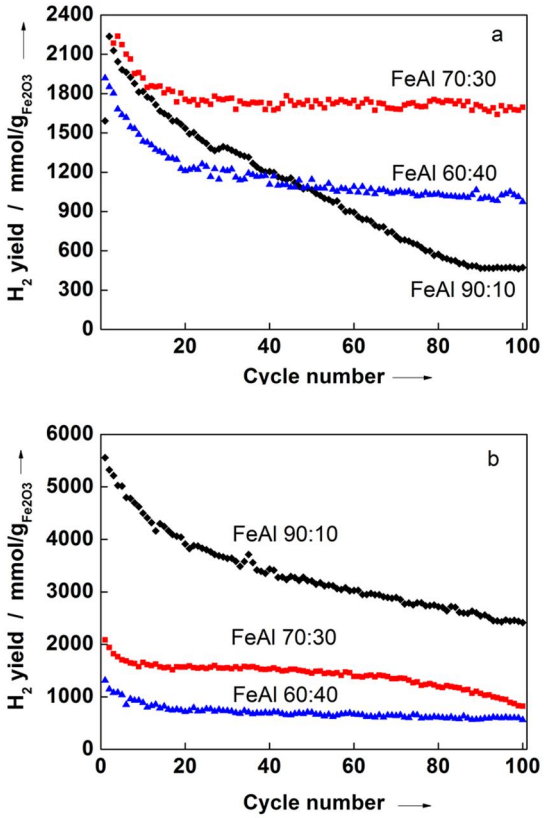

Figure 5. H_2 yield over 100 cycles for FeAl90:10, FeAl70:30 and FeAl60:40; at reaction temperature (a) 650 °C and (b) 750 °C.

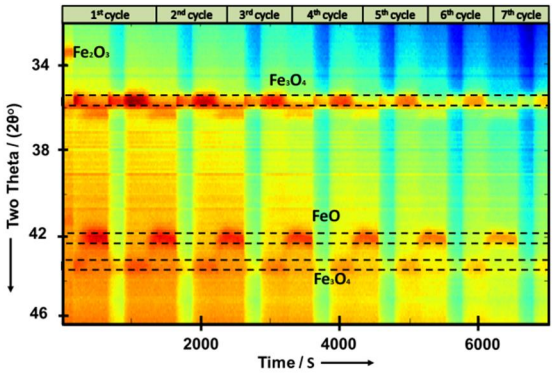

Figure 6. Time resolved 2D in-situ XRD pattern during 7 redox cycles at 650 °C for FeAl90:10.

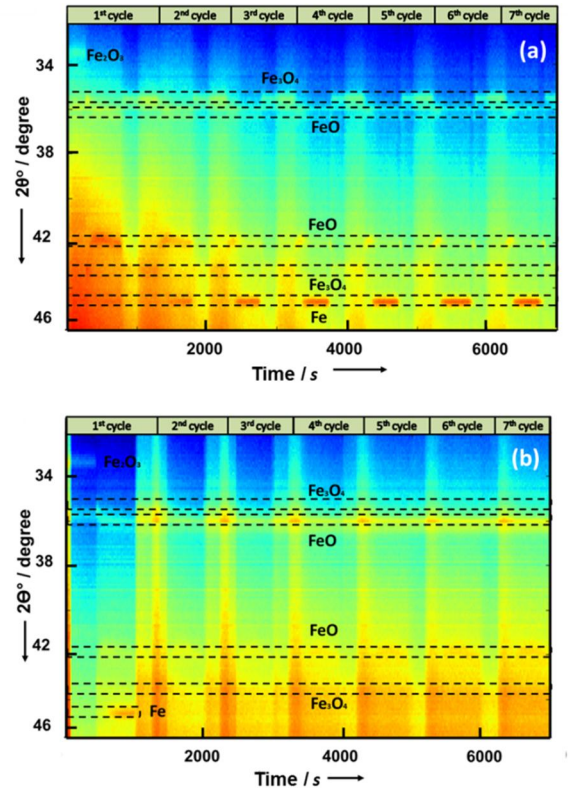

Figure 7. Time resolved 2D in-situ XRD pattern during 7 redox cycles at 750 °C for (a) FeAl90:10 and (b) FeAl70:30.

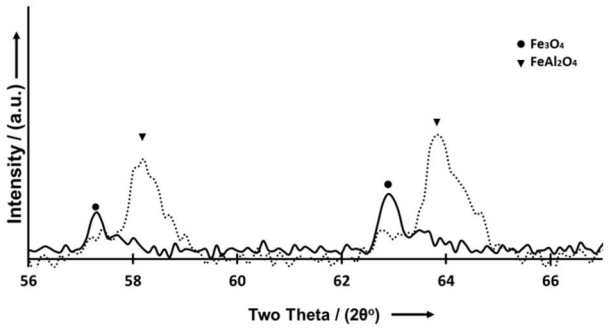

Figure 8. Magnification of the XRD pattern for samples FeAl90:10 (solid) and FeAl70:30 (dots) at 750 °C at the diffraction angle from 56°C to 67°.

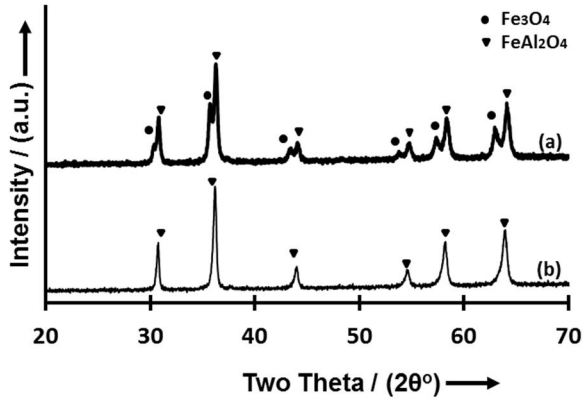

Figure 9. XRD pattern for the sample FeAl70:30 after 100 redox cycles (a) at 650 °C and (b) at 750 °C.

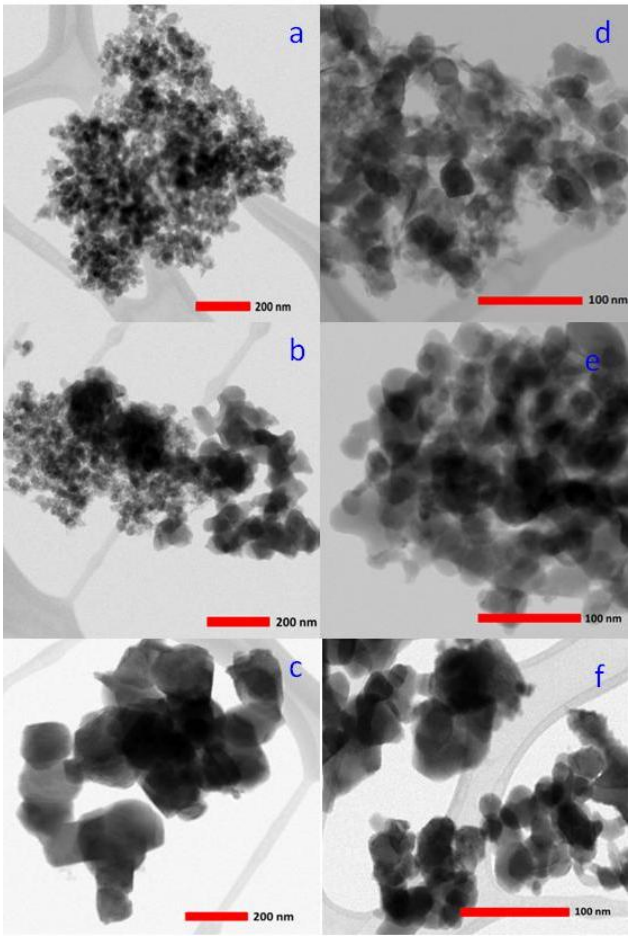

Figure 10. STEM images of (a) fresh FeAl90:10, and post reaction images after (b) 7 and (c) 100 cycles; The STEM images of FeAl70:30:(c) fresh and and after exposure to alternating H_2 and CO_2 environment after (e) 7 and (f) 100 cycles.

Table 1. Sample abbreviations and characterization.

Nominal Comp.	Sample name	Elemental Composition[a]		BET [m^2/g]		
Fe_2O_3 wt. %		Fe_2O_3 [wt. %]	Al_2O_3 [wt. %]	fresh	650°C [b]	750°C [b]
90	FeAl90:10	n.a.	n.a.	57	1.6	4.5
80	FeAl80:20	n.a.	n.a.	80	2.4	3.2
70	FeAl70:30	71.8	28.2	70	11	1.5
60	FeAl60:40	60.8	39.2	81	21	14

[a] calculated from the ICP-OES analysis [b] after the activity investigation for H_2O splitting (100 cycles).

Table 2. The particle size of the as prepared materials (Fe2O3) and for Fe3O4 after isothermal cycling as determined from XRD.

As prepared samples[a]	7 redox cycles[b]		100 redox cycles[b]	
[nm]	650°C [nm]	750°C [nm]	650°C [nm]	750°C [nm]
33±3.0	57±6.0	64±6.5	-	93±4.5
28±2.7	40±4.0	57±5.8	-	-
25±2.5	47±4.7	45±4.6	49±5.0	n.o
22±2.0	45±4.4	48±4.8	63±6.0	n.o

[a] particle size of Fe_2O_3. [b] particle size of Fe_3O_4 , n.o.: not observed

Table 3. Evolution of oxygen capacity.

Sample	Oxygen available in fresh Fe_3O_4	After complete phase transformation			Loss in oxygen storage capacity
		theoretical composition		oxygen available	
	[mmol/g]	Fe_3O_4 [mmol/g]	$FeAl_2O_4$ [mmol/g]	in Fe_3O_4 [mmol/g]	[%]
FeAl90:10	15.0	3.4	1.0	13.7	9
FeAl80:20	13.4	2.7	2.0	10.7	20
FeAl70:30	11.7	1.9	2.9	7.8	34
FeAl60:40	10.0	1.2	3.9	4.8	52